Carpio, J., Iglesias, I., Vera, M. & Sánchez, A. L. (2017). Critical slot size for deflagration initiation by hot products discharge into hydrogen–air atmospheres. *International Journal of Hydrogen Energy, 42*(2), 1298–1305.

Critical slot size for deflagration initiation by hot products discharge into hydrogen-air atmospheres

Jaime Carpio[a], Immaculada Iglesias[b], Marcos Vera[b,*], Antonio L. Sánchez[c]

[a]*Departamento de Ingeniería Energética, E.T.S. Ingenieros Industriales, José Gutiérrez Abascal 2, Universidad Politécnica de Madrid, 28006 Madrid, Spain*
[b]*Departamento de Ingeniería Térmica y de Fluidos, Universidad Carlos III de Madrid, 28911 Leganés, Spain*
[c]*Department of Mechanical and Aerospace Engineering, University of California, San Diego, 9500 Gilman Drive, La Jolla, CA 92093-0411, USA*

Abstract

This computational study addresses deflagration initiation of lean, stoichiometric, and moderately rich hydrogen-air mixtures by the sudden discharge of a hot planar jet of its adiabatic combustion products. The objective is to determine the minimum slot size required for ignition, a relevant quantity of interest for safety and technological applications concerning the accidental ignition of hydrogen. For sufficiently small jet velocities, the numerical solution of the problem requires integration of the two-dimensional Navier-Stokes equations for chemically reacting ideal-gas mixtures, supplemented by standard descriptions of the molecular transport terms and a reduced chemical-kinetic mechanism suitable for hydrogen-air combustion. The computations provide the variation of the critical slot size for hot-jet ignition with both the jet Reynolds number and the equivalence ratio of the mixture. In particular, it is seen that, while the Reynolds number exerts only a relatively weak effect on the ignition process, the influence of the equivalence ratio is much more pronounced, with the smallest slot widths found for stoichiometric, or slightly-rich conditions. The numerical results show three different ignition modes, with the flame developing from a clearly identified ignition kernel located either at the core of the leading vortex pair (mode 1), at the symmetry plane near the leading edge of the starting jet (mode 2), or at the jet stem connecting the jet exit with the starting vortex (mode 3).

Keywords: deflagration initiation, hydrogen-air mixtures, hot-jet ignition, transient jets, finite element method

---

*Corresponding author. Tel.: +34-916249987; fax: +34-916249430.
Email address: marcos.vera@uc3m.es (Marcos Vera)
URL: http://fluidosuc3m.es/people/mvcoello (Marcos Vera)

1. Introduction

It is well known that the combustion of a reactive mixture can be initiated by the sudden discharge of a hot jet of combustion products [1, 2]. The phenomenon is relevant in practical engineering applications, such as the hot-jet ignition systems investigated in [3], which can be utilized for ignition of ultra-lean fuel/air mixtures in both hydrogen-fred [4] and natural-gas [5] engines (see also [6] and references therein). There exists a minimum transverse size of the discharging jet, on the order of the planar defagration thickness and smaller than the quenching distance, above which ignition occurs [7]. This critical jet size has safety implications concerning the transport, handling, and storage of fuels, notably hydrogen [8, 9], for which combustion transmission between linked vessels or adjacent enclosures emerges as a key issue [10, 11]. For example, in the design of fameproof enclosures for electrical equipment [12] the permissible gaps must be sufficiently small to ensure that, if a reactive mixture enters the enclosure and becomes accidentally ignited by an electric spark or other ignition source, the resulting jet of escaping combustion products would not initiate a defagration in the surrounding combustible atmosphere. This has led to the classifcation of fammable gases and vapors into different groups based on the so-called maximum experimental safe gap [13, 14, 15].

In the case of axysimmetric jets, values of critical orifce radii for propane/air mixtures, measured in a specifc experimental facility, are available [16]. Also, the problem has been investigated for hydrogen-air mixtures by a combination of experimental and numerical methods [17, 18, 19, 20], providing increased understanding of the infuence of the jet temperature and mixing process on the occurrence of ignition. General infuences of jet Reynolds number and limiting-reactant diffusivity on critical ignition conditions have been recently addressed in computational work employing one-step Arrhenius chemistry along with constant transport properties [21]. While this simplifed model is useful in examining the general features of the interacting physicochemical phenomena, it is in general insufficient to yield accurate numerical quantifcations of critical ignition conditions for specifc fuel-air mixtures, which require more detailed combustion models. An example of these more involved computations is found in [22], where critical radii for lean and stoichiometric hydrogen-air mixtures were computed numerically using a standard description for the molecular transport together with a reliable reduced chemical-kinetic mechanism.

These previous works pertain to round jets. In many accidental scenarios, however, the discharge occurs through cracks or slits. Examples include micro-cracks in nuclear reactor

pressure vessels [23], pressurized hydrogen tank rupture [8] due to unusually fast crack growth induced by Hydrogen embrittlement [24], or gaps in metal or plastic housing of the "Flame-proof Enclosure" ignition protection type [12]. In those cases, the planar-jet configuration emerges as a more relevant model to represent the discharge process [25]. Numerical computations for the planar-jet configuration are presented below for the case of deflagration initiation of hydrogen-air mixtures at normal atmospheric conditions, providing predictions for the dependence of the critical slot width on the jet velocity and mixture composition. The results complement our previous computations for round jets [22] and extend the range of mixture compositions investigated previously by considering also moderately rich mixtures. The effect of thermal diffusion, which is known to play a relevant role in many hydrogen-combustion phenomena [26], is also assessed in the computations.

2. The model problem

A schematic representation of the planar configuration under study is shown in Fig. 1. An adiabatic flat wall separates a compartment containing a fresh mixture of hydrogen and air with equivalence ratio ϕ at normal atmospheric conditions ($p_0 = 1$ atm and $T_0 = 300$ K) from a compartment containing its adiabatic combustion products in equilibrium. For simplicity in the calculations, the air is assumed to be a binary mixture of oxygen and nitrogen with mass fractions $Y_{O_2,A} = 0.233$ and $Y_{N_2,A} = 0.767$. At the initial instant, a low-Mach-number stream of hot combustion products starts to discharge impulsively with uniform constant velocity U into the quiescent fresh mixture through a slot of semiwidth h, generating a developing variable-density planar jet that includes a leading starting vortex pair accompanied by an increasingly long jet stem [27].

The discharge process can be described numerically by integrating the Navier-Stokes equations for chemically reacting ideal-gas mixtures [28], with a low-Mach-number approximation

used when writing the energy equation and the equation of state

$$\frac{\partial \rho}{\partial t} + \mathbf{u} \cdot \nabla \rho = -\rho \nabla \cdot \mathbf{u}, \tag{1}$$

$$\rho \left(\frac{\partial \mathbf{u}}{\partial t} + \mathbf{u} \cdot \nabla \mathbf{u} \right) = -\nabla p + \nabla \cdot \left\{ \mu \left[\nabla \mathbf{u} + (\nabla \mathbf{u})^T \right] \right\}, \tag{2}$$

$$\rho \left(\frac{\partial Y_i}{\partial t} + \mathbf{u} \cdot \nabla Y_i \right) = -\nabla \cdot \mathbf{j}_i + \dot{m}_i, \qquad i = 1, \dots, I-1, \tag{3}$$

$$\rho c_p \left(\frac{\partial T}{\partial t} + \mathbf{u} \cdot \nabla T \right) = -\nabla \cdot \mathbf{q} - \sum_{i=1}^{I} h_i \dot{m}_i - \left(\sum_{i=1}^{I} \mathbf{j}_i c_{pi} \right) \cdot \nabla T, \tag{4}$$

$$p_0 = \rho \frac{R^\circ}{W} T. \tag{5}$$

In the above equations, $\mathbf{u}$ is the fluid velocity, p is the hydrodynamic pressure (accounting both for the spatial pressure variations and the isotropic component of the stress tensor), Y_i is the mass fraction of species i, and T is the fluid temperature. In addition, ρ is the density, μ the dynamic viscosity, $c_p = \sum_{i=1}^{I} c_{pi} Y_i$ the specific heat at constant pressure, p_0 the thermodynamic pressure (which is spatially uniform in low-Mach-number flows), $\mathbf{q}$ the heat flux vector, and $W = (\sum_{i=1}^{I} Y_i / W_i)^{-1}$ the molecular weight of the mixture. Regarding the I chemical species, h_i is the specific mass enthalpy, c_{pi} the specific heat at constant pressure, $\mathbf{j}_i$ the mass diffusion flux vector, and W_i the molecular weight of species i, while $\dot{m}_i$ stands for the net mass of species i produced per unit volume and unit time by the chemical reactions.

Following standard practice, the specific heat at constant pressure c_{pi} and the mass enthalpy h_i of species i, which are functions exclusively of the temperature, are computed using the NASA polynomials [29]. The Fourier law is used to evaluate the heat flux vector

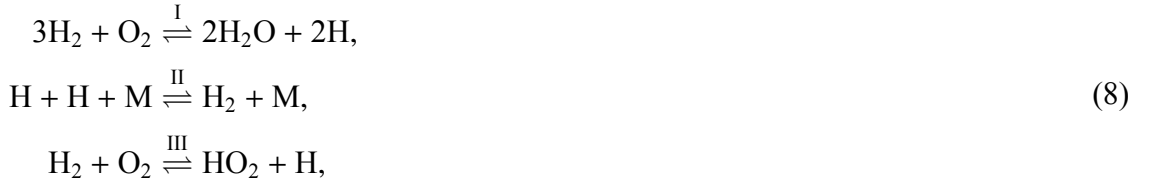$$\mathbf{q} = -\lambda \nabla T, \tag{6}$$

and a generalized Fick law provides the species diffusion flux vector as follows

$$\mathbf{j}_i = \rho Y_i \left(-\frac{D_i}{X_i} \nabla X_i + \frac{D_i \theta_i}{X_i} \frac{\nabla T}{T} + V_c \right), \tag{7}$$

where the diffusion velocity is written in terms of three components representing, respectively, the ordinary diffusion velocity (expressed in terms of the gradient of the species molar fractions X_i), the thermal diffusion velocity, and a correction velocity, V_c, defined so that the restriction $\sum_{i=1}^{I} \mathbf{j}_i = \mathbf{0}$ is satisfied. Standard mixture-averaged methods [30, 31] are used to evaluate the transport properties of the gas mixture, including the dynamic viscosity of the mixture μ, the thermal conductivity λ, and the species diffusivities D_i, with Soret diffusion included for H and

H$_2$ in the computations reported below. In particular, the thermal diffusion ratios, θ_i, are set to zero for species other than the light species H and H$_2$, a well justifed approach adopted in most hydrogen-air combustion studies [26, 32].

As in our previous work [22], we adopt here the three-step reduced chemical-kinetic mechanism proposed by Boivin et al. [33], which is known to provide accurate results under a wide range of conditions including autoignition and defagration propagation. This reduced mechanism has been recently used to describe accurately autoignition of hydrogen in high-speed turbulent jets [34], which makes it particularly suitable for the problem at hand. The three-step mechanism includes a branching reaction (I), a recombination reaction (II), and an initiation reaction (III)

$$
\begin{aligned}
3\text{H}_2 + \text{O}_2 &\overset{\text{I}}{\rightleftharpoons} 2\text{H}_2\text{O} + 2\text{H}, \\
\text{H} + \text{H} + \text{M} &\overset{\text{II}}{\rightleftharpoons} \text{H}_2 + \text{M}, \\
\text{H}_2 + \text{O}_2 &\overset{\text{III}}{\rightleftharpoons} \text{HO}_2 + \text{H},
\end{aligned}
\tag{8}
$$

involving $I - 1 = 5$ reacting species, i.e., H$_2$, O$_2$, H, HO$_2$, and H$_2$O. This kinetic mechanism provides the chemical source terms $\dot{m}_i$ appearing in the species conservation equations, with the reaction rates w_I, w_II and w_III computed in terms of the temperature and species mass fractions according to the guidelines provided in [33], and with the reaction constants taken from the San Diego mechanism [35]. The mass fraction of the I-th species, the abundant inert nitrogen gas, is readily computed from overall mass conservation as $Y_{\text{N}_2} = 1 - \sum_{i=1}^{I-1} Y_i$.

The initial composition of the fresh mixture is defned by the equivalence ratio ϕ, which also determines the temperature and composition of the hot burnt mixture in the jet through an a-priori equilibrium calculation using the GASEQ code [36]

$$
x = 0, \quad 0 < y < h: \quad \mathbf{u} = U\mathbf{e}_x, \quad Y_i = Y_{ib}(\phi), \quad T = T_b(\phi).
\tag{9}
$$

The values of Y_{ib} and T_b are listed in Table 1 for the range of equivalence ratios under study. Additional boundary conditions for the numerical integrations include an adiabatic impermeable wall

$$
x = 0, \quad y > h: \quad \mathbf{u} = 0, \quad \mathbf{j}_i \cdot \mathbf{n} = 0, \quad \mathbf{q} \cdot \mathbf{n} = 0,
\tag{10}
$$

a zero fux condition at the symmetry plane

$$
x > 0, \quad y = 0: \quad \mathbf{u} \cdot \mathbf{e}_y = 0, \quad \mathbf{j}_i \cdot \mathbf{n} = 0, \quad \mathbf{q} \cdot \mathbf{n} = 0,
\tag{11}
$$

5

and an outflow condition for the velocity and pressure far from the orifice

$$x \to \infty, \quad y \to \infty: \quad \left\{ -p + \mu \left[\nabla \mathbf{u} + (\nabla \mathbf{u})^T \right] \right\} \cdot \mathbf{n} = \mathbf{0}, \quad \mathbf{j}_i \cdot \mathbf{n} = 0, \quad \mathbf{q} \cdot \mathbf{n} = 0, \quad (12)$$

where the composition and temperature are those of the unburnt mixture.

A space-adaptive finite element method, used also in our previous work [22], was employed for the numerical integration. Due to the slender shape of high Reynolds number jets and the development of thin mixing layers surrounding the jet head, anisotropic mesh elements are used in the space discretization in combination with local adaptive mesh refinement [37], with the size of the smallest elements, located at the jet mixing layer, limited to a hundredth of the orifice semiwidth h. The use of anisotropic mesh adaptation constitutes a major improvement with respect to our earlier work [22], which reduces the number of nodes required for the simulations and significantly increases the efficiency of computing. Two meshes obtained in a sample case computed with anisotropic and isotropic adaptation are compared in Fig. 2. Although the number of elements of the anisotropically adapted mesh is only 20% smaller than in the corresponding isotropic mesh, the computational speed-up factor, evaluated from the start of the jet discharge to the instant shown in figure, is close to 2.4. In brief, the anisotropic mesh is best suited to the characteristics of the flow, which leads to system matrices that are better conditioned and linear systems that require a significantly smaller number of iterations to be solved.

The time discretization scheme uses a semi-Lagrangian-Galerkin method to treat the convective terms, whereas the diffusion-reaction terms are discretized using a second-order explicit Runge-Kutta-Chebyshev scheme with a variable number of stages that is adaptively changed in time. Further details on the numerical method and its application to low-Mach transient combustion problems can be found elsewhere [38]. The equations (1)–(4) were integrated with a small constant time step $\Delta t = 0.05 h/U$ in a rectangular integration domain with width $100h$ and streamwise length up to $500h$. Different time steps and also different minimum element sizes were employed in sample computations to check the independence of the results with the selected discretization.

3. Numerical results

Besides the equivalence ratio ϕ, the solution depends on the values of h and U, with the dependence on the latter being conveniently expressed through a jet Reynolds number

$Re = \rho_u U h/\mu_u$, where ρ_u and μ_u denote the density and viscosity of the unburnt mixture. For given values of ϕ and Re, there exists a critical value of the slot semiwidth, h_c, above which a deflagration forms as a result of the jet discharge.

Two series of snapshots corresponding to typical subcritical and supercritical ignition events are illustrated in Fig. 3. The two panels display isocontours of temperature and H-atom mass fraction obtained for $\phi = 0.7$ and $Re = 250$ at different times t, conveniently scaled with the residence time h/U, whereas the axial and transverse coordinates are scaled with the slot semi-width h. The left-hand-side snapshots are computed for $h = 0.0270$ mm, slightly below the critical value $h_c = 0.0271$ mm corresponding to these conditions. As a result, the products in the jet mix with the ambient fresh mixture without significant chemical reaction, generating for large times a radical-free slender steady jet. The right-hand-side snapshots in Fig. 3 correspond to $h = 0.0272$ mm $> h_c = 0.0271$ mm. In the initial stages following the jet discharge, the hot products mix with the fresh mixture without appreciable chemical heat release, giving for $t/(h/U) = 800$ a temperature distribution very similar to that found in the accompanying subcritical computation. The effect of chemical reaction begins to modify the temperature field at later times, as can be seen in the plots for $t/(h/U) = 900$ and, to a larger extent, for $t/(h/U) = 1000$, with a clear ignition kernel identified by the H-atom presence in the core of the leading vortex. Combustion spreads from this kernel in the form of a relatively thick flame front that propagates in all directions, as indicated by the isocontours for $t/(h/U) > 1000$.

It is worth mentioning that the snapshots in Fig. 3 represent only one of the manners in which ignition can be observed to develop in these hydrogen-air systems (mode 1). This ignition mode is also found for other values of ϕ and Re, as shown by the computations of Fig. 4a, corresponding to $\phi = 0.4$ and $Re = 500$. By contrast, the computations shown in Fig. 4b reveal that for the same equivalence ratio ignition for $Re = 250$ occurs instead at the symmetry plane near the leading edge of the starting jet (mode 2). The ignition front propagates then laterally along the mixing layer that surrounds the jet head, in the form of an edge flame [39] assisted by the induced vortex motion. Reducing the Reynolds number to sufficiently small values also changes the observed behavior. For instance, Fig. 4c shows that for $Re = 100$ and $\phi = 0.7$ the starting vortex plays a secondary role and the flame develops rather as a result of ignition in the trailing jet stem connecting the jet exit with the leading vortex (mode 3). Detailed videos of the jet discharge process illustrating failed and successful initiation events for various Reynolds numbers and equivalence ratios, including the cases shown in Figs. 3 and 4, are provided as

supplementary material.

Extensive numerical computations for fixed values of ϕ and Re and incrementally increasing values of h were carried out to determine the critical slot semiwidth h_c in the parametric ranges $100 \leq Re \leq 500$ and $0.3 \leq \phi \leq 1.5$, with results summarized in Fig. 5. The left plot shows the variation of h_c with ϕ for different values of Re, whereas the right plot shows the variation of h_c with U for different values of Re and ϕ. As can be seen, for a given Re there exists a pronounced variation of h_c with the composition, with the minimum value of h_c occurring at approximately stoichiometric conditions ($\phi \simeq 1 - 1.1$), just like the quenching distance [40]. For the range of ϕ shown in the figure, the largest value of h_c (~ 0.27 mm) is found for $\phi = 0.3$. Reducing the value of ϕ further leads to even larger values of h_c that diverge as ϕ approaches $\phi = 0.25$, the chemical-kinetic limit at which the crossover temperature of atmospheric hydrogen-air combustion is reached, so that for smaller temperatures chain-branching ignition is precluded [26].

The left plot of Fig. 5 also provides information regarding the ignition modes observed in the numerical integrations, with different symbols used to indicate conditions under which modes 1, 2, and 3 prevail. As can be seen, mode 1 dominates for the larger Reynolds numbers ($Re = 250$ and 500) for all except the lower equivalence ratios ($\phi \lesssim 0.4$ for $Re = 250$, and $\phi \lesssim 0.3$ for $Re = 500$) for which mode 2 takes over. For the lowest Reynolds number ($Re = 100$) mode 2 is still observed at low equivalence ratios ($\phi \lesssim 0.4$), and also for near stoichiometric mixtures ($0.9 \lesssim \phi \lesssim 1.3$), whereas for moderately lean ($0.5 \lesssim \phi \lesssim 0.8$) and rich ($1.4 \lesssim \phi$) mixtures ignition occurs at the trailing jet according to mode 3.

For a given value of ϕ, the critical slot width increases mildly with the Reynolds number, although the variation is not very pronounced. For instance, for stoichiometric mixtures ($\phi = 1$) the numerical computations yield $h_c = (0.0066, 0.0127, 0.0141)$ mm for $Re = (100, 250, 500)$, respectively. Indeed, as the Reynolds number grows the critical slot size becomes less and less dependent on Re, so that critical slot semiwidth vs. equivalence ratio curves for larger values of Re are expected to be very similar to those reported in Fig. 5 (left) for $Re = 500$, as long as the flow remains laminar and sufficiently subsonic.

It is interesting to note that the critical slot semiwidth h_c is significantly smaller than the critical jet radius a_c computed in axisymmetric configurations [22], the value of h_c being roughly one-half of a_c for low equivalence ratios, and up to one-fourth for near stoichiometric mixtures. This finding is in qualitative agreement with the observation that measured quenching

diameters for round tubes are about 50% larger than the quenching distance in parallel-plate configurations [41].

Particularly relevant for safety issues, the critical slot widths computed here (e.g., $2h_c = 0.0282$ mm for $\phi = 1$ and $Re = 500$) are much lower than the published hydrogen quenching distance of $0.05 - 0.64$ mm [41, 42]. They are also significantly smaller than the maximum experimental safe gap (MESG) reported in the literature, which ranges from 0.08 to 0.28 mm depending on the experimental apparatus used for testing [43]. This is probably a consequence of the absence of heat losses to the slot walls, which have been ignored in our simulations in contrast with the experimental apparatus for determining the MESG, which features flat metal joints 25 mm width which remove a significant amount of the thermal energy of the hot gases issuing from the enclosure.

Compressibility effects, which were not accounted for in our computations, are increasingly important for increasing injection velocities and can no longer be neglected when the jet velocity becomes comparable to the ambient sound speed c_u. To help assessing the importance of this effect, the right-hand-side plot in Fig. 5 includes lines of constant Mach number $Ma = U/c_u$. The incompressible computations presented are accurate for sufficiently small values of Ma, corresponding to the points towards the left-hand side of the plot. Modifications to the resulting values of h_c are expected to arise as Ma increases. For these cases, the associated transient computation should account for counteracting effects of the waves generated at the initial instant (i.e., a shock wave traveling into the fresh mixture and an accompanying expansion wave that propagates upstream from the slot into the burnt mixture). Such an analysis has been carried out in a closely related configuration by Radulescu and coworkers [44, 45, 46], who studied the release of pressurized hydrogen gas at room temperature into ambient air, and the shock-induced ignition of the resulting one-dimensional unsteady mixing layer of fuel and oxidizer at the jet head. However, their results can not be easily extrapolated to our analysis of deflagration initiation by hot products discharge.

The relevance of Soret diffusion in these hot-jet ignition events was assessed in computations by removing selectively the associated terms in the diffusion flux. Contrary to expectations, the effect is only mild. The values of h_c obtained without accounting for thermal diffusion of H and H_2 tend to be larger, but the differences observed never exceed 10%, with the effect being somewhat more noticeable for leaner mixtures and smaller Reynolds numbers. Although the number of simulations carried out without Soret effect was small, none of them showed

9

changes in the mode of ignition due to the lack of thermal diffusion.

To asses the effect of non-impulsive jet discharge, numerical simulations of def agration initiation by transient hot jets were also carried out in the case $Re = 500$ and $\phi = 0.5$ with the jet velocity increasing linearly from $u = 0$ at $t = 0$ to $u = U$ at $t = t_r$ for three non-dimensional rising times $t_r/(h/U) = (1, 10, 25)$. The numerical results show that increasing the dimensionless rising time from 0 to 25 decreases the critical slot semiwidth from 0.06 mm to 0.055 mm, resulting in a reduction of the critical slot size of less than 10%. As a result, increasing the rising time has qualitatively the same effect than decreasing the Reynolds number.

Larger values of the injection velocity, for which compressibility effects are likely to be relevant, and also larger values of the chamber pressure $p_0 > 1$ atm and elevated initial temperatures $T_0 > 300$ K, are also of interest for hydrogen safety applications. Clearly, these issues are worth investigating in future numerical and experimental studies. This study could also be improved if experimental data were available to validate the numerical results. However, due to the small size of the critical slot widths predicted by the simulations (between 13 and 540 microns in the parametric range considered here), large difficulties are anticipated in carrying out the required experiments, since in the case of hydrogen-air mixtures critical slot sizes are much smaller than those of hydrocarbon-air (e.g., propane-air) mixtures, already tested in the literature [16].

4. Conclusions

Numerical integrations incorporating realistic descriptions for molecular transport and chemical kinetics have been used to determine the critical slot semiwidth h_c for ignition of a hydrogen-air mixture by a sudden planar jet discharge of its adiabatic combustion products. Atmospheric normal conditions $p_0 = 1$ atm and $T_0 = 300$ K were selected for the mixture, as they are of direct interest for safety studies concerning the accidental ignition of hydrogen. The variation of h_c with the injection velocity and equivalence ratio is calculated assuming negligible compressibility effects, giving the results summarized in Fig. 5, of direct interest for safety applications.

The numerical results show, in particular, the existence of three different ignition modes, with the ignition kernel located at the core of the leading vortex pair (mode 1), at the symmetry plane near the leading edge of the starting jet (mode 2), or at the jet stem connecting

10

the jet exit with the starting vortex (mode 3). The computed values of h_c are signif cantly smaller than the critical jet radius a_c previously reported in axisymmetric conf gurations, h_c being approximately one-half of a_c for low equivalence ratios, and up to one-fourth for near stoichiometric conditions. Finally, non-impulsive jet discharge obtained with linear ramp up velocity programs of growing rising times are observed to have qualitatively the same effect than decreasing the Reynolds number, leading to a slight reduction of the critical slot size.

Acknowledgements

List of table captions

Table 1. Temperature and composition of the adiabatic reaction products in the burnt mixture as a function of the equivalence ratio.

List of f gure captions

Figure 1. Schematic representation of the problem showing the computational domain used for integration.

Figure 2. Anisotropic (8531 elements, top) and isotropic (10526 elements, bottom) adapted meshes for $Re = 500$ and $\phi = 0.8$, corresponding to a marginally supercritical successful initiation event with $h = 0.02119$ mm ($> h_c = 0.02069$ mm) at $t/(h/U) = 250$.

Figure 3. Snapshots of temperature (upper isocontours) and H-atom mass fraction (lower isocontours) corresponding to failed ($h = 0.0270$ mm: left-hand-side panel) and successful ($h = 0.0272$ mm: right-hand-side panel) initiation events for $\phi = 0.7$ and $Re = 250$. The plots show temperature isocontours corresponding to $(2, 3, 4, 5, 6, 7) \times 300$ K and H-atom mass fraction isocontours corresponding to $(0.1, 0.2, \ldots, 0.9) \times Y_{H,\max}$ for different times, scaled in the labels with the residence time h/U. Axial and transverse coordinates are scaled with the slot semiwidth h, with minor (major) ticks spaced by $10h$ ($50h$). The maximum computed H-atom mass fraction is $Y_{H,\max} = 2.412 \times 10^{-3}$.

Figure 4. Snapshots of temperature (upper isocontours) and H-atom mass fraction (lower isocontours) corresponding to marginally supercritical successful initiation events in the three ignition modes identif ed in this study: a) mode 1: $\phi = 0.4$, $Re = 500$, $h = 0.1097$ mm, $Y_{H,\max} = 9.728 \times 10^{-4}$; b) mode 2: $\phi = 0.4$, $Re = 250$, $h = 0.09726$ mm, $Y_{H,\max} = 8.410 \times 10^{-4}$; and c) mode 3: $\phi = 0.7$, $Re = 100$, $h = 0.0187$ mm, $Y_{H,\max} = 1.870 \times 10^{-3}$. For further details see caption of Fig. 3.

Figure 5. Variation of the critical slot semiwidth h_c with the equivalence ratio (left) and jet velocity (right). The left plot shows error bars indicating the marginal subcritical and supercritical values of h determined numerically, with h_c def ned as the average of both values. The right plot is limited to cases with $\phi \leq 1.1$. The ignition modes observed in the numerical integrations are indicated by the symbols specif ed in the f gure legend.

References

[1] Wolfhard HG. The ignition of combustible mixtures by hot gases. J Jet Propulsion 1958;28(12):798–804.

[2] Phillips H. Ignition in a transient turbulent jet of hot inert gas. Combust Flame 1972;19(2):187–195.

[3] Murase E, Ono S, Hanada K, Oppenheim AK. Initiation of combustion in lean mixtures by f ame jets. Combust Sci Technol 1996;113(1):167–177.

[4] Boretti AA, Watson HC. Enhanced combustion by jet ignition in a turbocharged cryogenic port fuel injected hydrogen engine. Int J Hydrogen Energ 2009;34(5):2511–2516.

[5] Reddy H, Abraham J. Ignition kernel development studies relevant to lean-burn natural-gas engines. Fuel 2010;89(11):3262–3271.

[6] Biswas S, Tanvir S, Wang H, Qiao L. On ignition mechanisms of premixed CH 4/air and H 2/air using a hot turbulent jet generated by pre-chamber combustion. Appl Therm Eng 2016;106:925–937.

[7] Phillips H. On the transmission of an explosion through a gap smaller than the quenching distance. Combust Flame 1963;7:129–135.

[8] Rigas F, Sklavounos S. Evaluation of hazards associated with hydrogen storage facilities. Int J Hydrogen Energ 2005;30:1501–1510.

[9] Najjar YS. Hydrogen safety: The road toward green technology. Int J Hydrogen Energ 2013;38(25):10716–10728.

[10] Thibault P, Liu YK, Chan C, Lee JH, Knystautas R, Guirao C, Hjertager B, Fuhre K. Transmission of an explosion through an orif ce. P Combust Inst 1982;19(1):599–606.

[11] Razus D, Oancea D, Chirila F, Ionescu NI. Transmission of an explosion between linked vessels. Fire Safety J 2003;38(2):147–163.

[12] IEC 60079-1:2003(E) (International Standard), Electrical Apparatus for Explosive Gas Atmospheres – Part 1: Flameproof Enclosures "d", International Electrotechnical Commission, Geneva, 2003.

[13] Strehlow RA, Nicholls JA, Magison EC, Schram PJ. An investigation of the maximum experimental safe gap anomaly. J Hazard Mater 1979;3(1):1–15.

[14] Phillips H. The physics of the maximum experimental safe gap. In Proceedings of the International Symposium on the Explosion Hazard Classif cation of Vapors, Gases, and Dusts, pp. 65–82. National Academy Press, Vol. 447, 1987.

[15] Phillips H. A Comparison of "Standard" Methods for the Determination of Maximum Experimental Safe Gap (MESG). In Proceedings of the International Symposium on the Explosion Hazard Classif cation of Vapors, Gases, and Dusts, pp. 83–108. National Academy Press, Vol. 447, 1987.

[16] Larsen Ø, Eckhoff RK. Critical dimensions of holes and slots for transmission of gas explosions: Some preliminary results for propane/air and cylindrical holes. J Loss Prev Proc Ind, 2000;13(3):341–347.

[17] Sadanandan R, Markus D, Schießl R, Maas U, Olofsson J, Seyfried H, Richter M, Aldén M. Detailed investigation of ignition by hot gas jets. P Combust Inst 2007;31(1):719–726.

[18] Sadanandan R, Schießl RA, Markus D, Maas U. 2D mixture fraction studies in a hot-jet ignition conf guration using NO-LIF and correlation analysis. Flow, Turbulence and Combustion, 2011;86:45–62.

[19] Ghorbani A, Steinhilber G, Markus D, Maas U. Numerical investigation of ignition in a transient turbulent jet by means of a PDF method. Combust Sci Technol 2014;186:1582–1596.

[20] Ghorbani A, Markus D, Steinhilber G, Maas U. A numerical approach to investigate the maximum permissible nozzle diameter in explosion by hot turbulent jets. J Loss Prevent Proc 2015;36:539–543.

[21] Iglesias I, Vera M, Sánchez AL, Liñán A. Numerical analyses of def agration initiation by a hot jet. Combust Theor Model 2012;16(6):994–1010.

[22] Carpio J, Iglesias I, Vera M, Sánchez AL, Liñán A. Critical radius for hot-jet ignition of hydrogen-air mixtures. Int J Hydrogen Energ 2013;38(7):3105–3109.

[23] Knott JF. Structural integrity of nuclear reactor pressure vessels. Philos Mag 2013;93:3835–3862.

[24] Yurioka N, Suzuki H. Hydrogen assisted cracking in C-Mn and low alloy steel weldments. Int Mater Rev 1990;35:217–249.

[25] Lim KB, Chao BH, Sunderland PB, Axelbaum RL. A theoretical study of spontaneous ignition of fuel jets in an oxidizing ambient with emphasis on hydrogen jets. Combust Theor Model 2008;12:1179–1196.

[26] Sánchez AL, Williams FA. Recent advances in understanding of f ammability characteristics of hydrogen. Prog Energ Combust 2014;41:1–55.

[27] Iglesias I, Vera M, Sánchez AL, Liñán A. Simulations of starting gas jets at low Mach numbers. Phys Fluids 2005;17:038105.

[28] Williams FA. Combustion Theory. 2nd ed. Redwood City: Addison-Wesley; 1985.

[29] Smith GP, Golden DM, Frenklach M, Moriarty NW, Eiteneer B, Goldenberg M, Bowman CT, Hanson RK, Song S, Gardiner WC, Lissianski VV, Qin Z. GRI-Mech 3.0; 1999. `http://combustion.berkeley.edu/gri_mech/data/nasa_plnm.html`

[30] Dixon-Lewis G. Flame structure and f ame reaction kinetics II. Transport phenomena in multicomponent systems. P Roy Soc Lond A Mat 1968;307:111–135.

[31] Kee RJ, Dixon-Lewis G, Warnatz J, Coltrin ME, Miller JA. A Fortran computer code package for the evaluation of gas-phase, multicomponent transport properties. Albuquerque, NM: Sandia National Laboratories, Report SAND 86-8246; 1986.

[32] Fristrom RM, Monchick L. Two simple approximations to the thermal diffusion factor and their applications to f ame studies. Combust Flame 1988;71(1):89–99.

[33] Boivin P, Jiménez C, Sánchez AL, Williams FA. An explicit reduced mechanism for H_2-air combustion. P Combust Inst 2011;33(1):517–523.

[34] Boivin P, Dauptain A, Jiménez C, Cuenot B. Simulation of a supersonic hydrogen-air autoignition-stabilized f ame using reduced chemistry. Combust Flame 2012;159(4):1779–1790.

[35] Saxena P, Williams FA. Testing a small detailed chemical-kinetic mechanism for the combustion of hydrogen and carbon monoxide. Combust Flame 2006;145(1):316–323.

[36] Morley C. GASEQ: Chemical equilibria in perfect gases, Version 0.79, http://www.gaseq.co.uk/; Jan 2005.

[37] Carpio J, Prieto JL. An anisotropic, fully adaptive algorithm for the solution of convection-dominated equations with semi-Lagrangian schemes. Comput Method Appl M 2014;273:77–99.

[38] Carpio J, Prieto JL, Vera M. A local anisotropic adaptive algorithm for the solution of low-Mach transient combustion problems. J Comput Phys 2016;306:19–42.

[39] Buckmaster J. Edge-f ames. Prog Energ Combust 2002;28:435–475.

[40] Jung Y, Lee MJ, Kim NI. Direct prediction of laminar burning velocity and quenching distance of hydrogen-air f ames using an annular stepwise diverging tube (ASDT). Combust Flame 2016;164:397–399.

[41] Potter AE. Flame Quenching. In Progress in Combustion Science and Technology, vol. I, pp. 145–181, Pergamon Press, New York, 1960.

[42] Lewis B, Von Elbe G. Combustion, f ames and explosions of gases, 3rd Ed., Academic Press, Orlando, Florida, 2012.

[43] Britton LG. Using maximum experimental safe gap to select f ame arresters. Process Saf Prog 2000;19(3):140–145.

[44] Radulescu MI, Law CK. The transient start of supersonic jets. J Fluid Mech 2007;578:331–369.

[45] Maxwell BM, Radulescu MI. Ignition limits of rapidly expanding diffusion layers: Application to unsteady hydrogen jets. Combust Flame 2011;158(10):1946–1959.

[46] Maxwell BM, Tawagi P, Radulescu MI. The role of instabilities on ignition of unsteady hydrogen jets f owing into an oxidizer. Int J Hydrogen Energ 2013;38(6):2908–2918.

Tables

Table 1: Temperature and composition of the adiabatic reaction products in the burnt mixture as a function of the equivalence ratio.

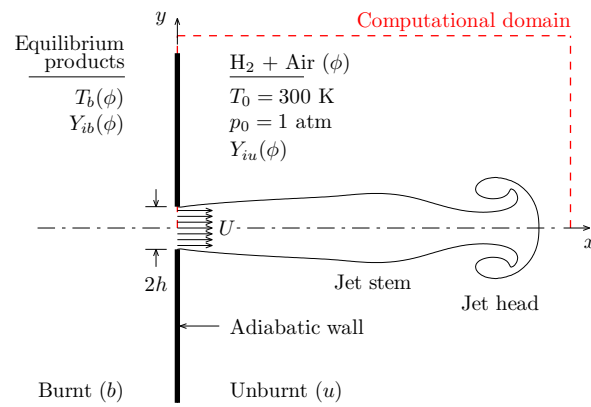| ϕ	T_b	$Y_{H_2 b}$	$Y_{O_2 b}$	Y_{Hb}	$Y_{HO_2 b}$	$Y_{H_2 O b}$
0.30	1189	2.353×10^{-10}	1.631×10^{-1}	3.332×10^{-13}	1.433×10^{-8}	6.990×10^{-2}
0.35	1311	3.006×10^{-9}	1.515×10^{-1}	9.864×10^{-12}	5.035×10^{-8}	8.155×10^{-2}
0.40	1428	2.342×10^{-8}	1.398×10^{-1}	1.489×10^{-10}	1.355×10^{-7}	9.320×10^{-2}
0.50	1647	5.351×10^{-7}	1.165×10^{-1}	8.930×10^{-9}	5.735×10^{-7}	1.165×10^{-1}
0.60	1849	5.345×10^{-6}	9.325×10^{-2}	1.721×10^{-7}	1.510×10^{-6}	1.398×10^{-1}
0.70	2034	3.202×10^{-5}	7.017×10^{-2}	1.623×10^{-6}	2.860×10^{-6}	1.628×10^{-1}
0.80	2198	1.360×10^{-4}	4.775×10^{-2}	9.238×10^{-6}	4.087×10^{-6}	1.852×10^{-1}
0.90	2333	4.487×10^{-4}	2.715×10^{-2}	3.481×10^{-5}	4.266×10^{-6}	2.057×10^{-1}
1.00	2420	1.243×10^{-3}	1.066×10^{-2}	8.916×10^{-5}	2.790×10^{-6}	2.220×10^{-1}
1.10	2431	3.032×10^{-3}	2.222×10^{-3}	1.489×10^{-4}	8.979×10^{-7}	2.300×10^{-1}
1.20	2391	5.675×10^{-3}	4.336×10^{-4}	1.709×10^{-4}	2.349×10^{-7}	2.312×10^{-1}
1.30	2343	8.509×10^{-3}	1.185×10^{-4}	1.683×10^{-4}	7.698×10^{-8}	2.309×10^{-1}
1.40	2298	1.137×10^{-2}	4.057×10^{-5}	1.562×10^{-4}	2.983×10^{-8}	2.303×10^{-1}
1.50	2254	1.422×10^{-2}	1.590×10^{-5}	1.406×10^{-4}	1.282×10^{-8}	2.296×10^{-1}

Figures

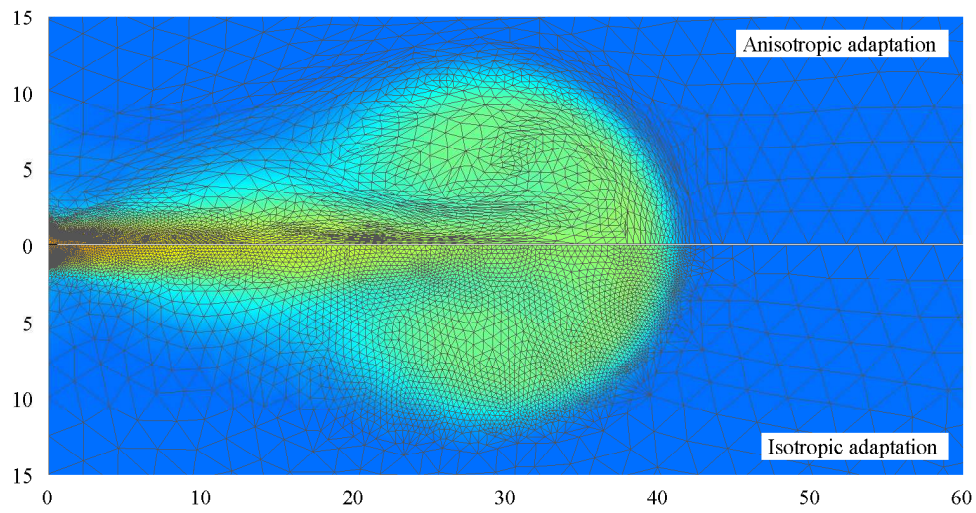Figure 1: Schematic representation of the problem showing the computational domain used for integration.

Figure 2: Anisotropic (8531 elements, top) and isotropic (10526 elements, bottom) adapted meshes for $Re = 500$ and $\phi = 0.8$, corresponding to a marginally supercritical successful initiation event with $h = 0.02119$ mm ($> h_c = 0.02069$ mm) at $t/(h/U) = 250$.
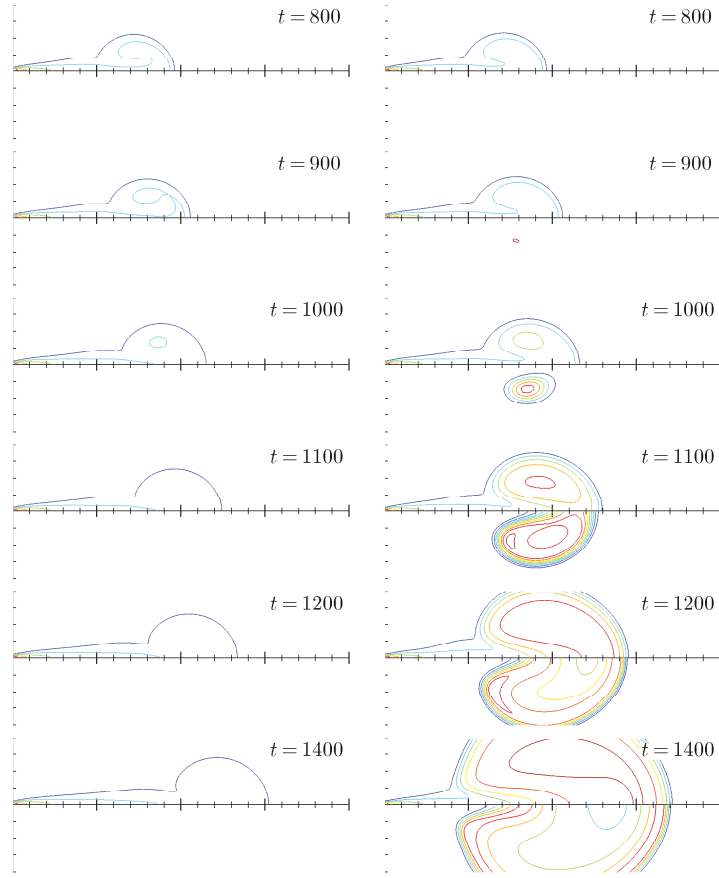
Figure 3: Snapshots of temperature (upper isocontours) and H-atom mass fraction (lower isocontours) corresponding to failed ($h = 0.0270$ mm: left-hand-side panel) and successful ($h = 0.0272$ mm: right-hand-side panel) initiation events for $\phi = 0.7$ and $Re = 250$. The plots show temperature isocontours corresponding to $(2, 3, 4, 5, 6, 7) \times 300$ K and H-atom mass fraction isocontours corresponding to $(0.1, 0.2, \ldots, 0.9) \times Y_{\mathrm{H,max}}$ for different times, scaled in the labels with the residence time h/U. Axial and transverse coordinates are scaled with the slot semiwidth h, with minor (major) ticks spaced by $10h$ ($50h$). The maximum computed H-atom mass fraction is $Y_{\mathrm{H,max}} = 2.412 \times 10^{-3}$.
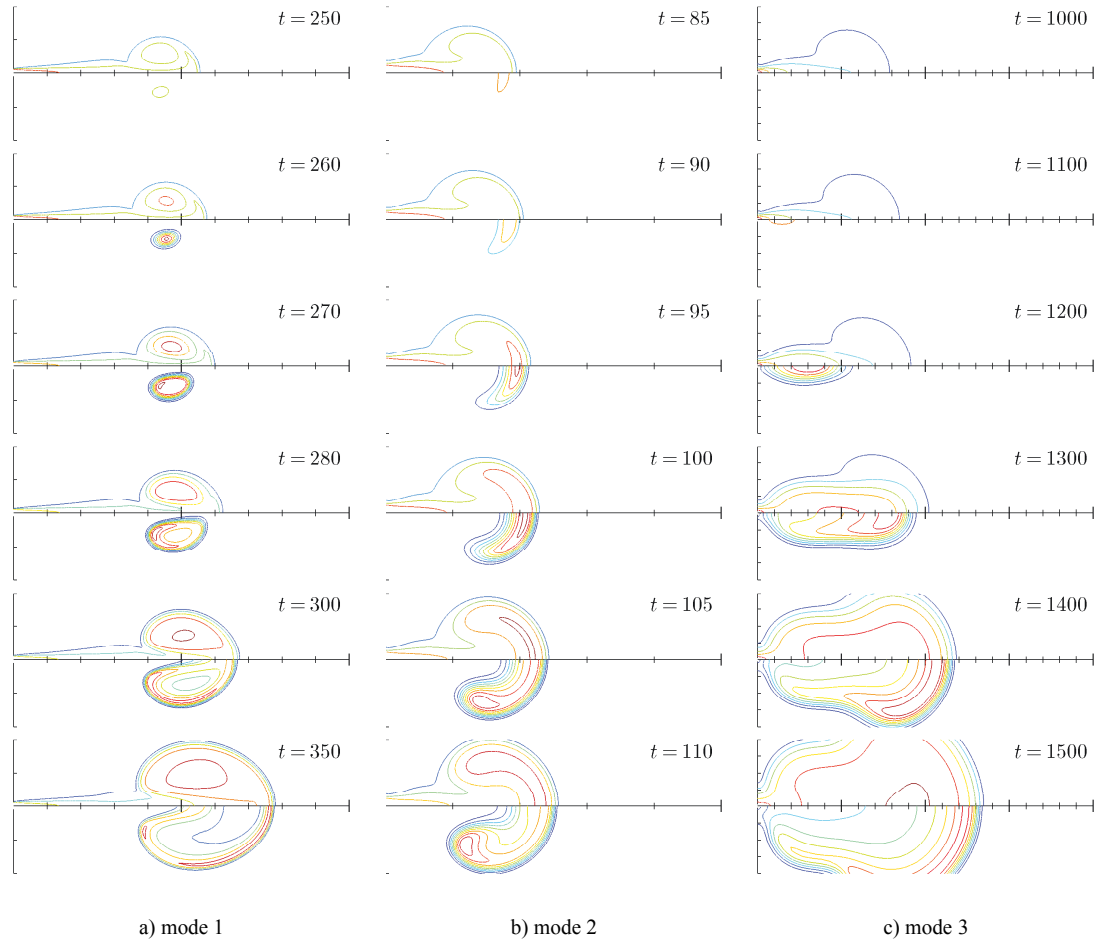
Figure 4: Snapshots of temperature (upper isocontours) and H-atom mass fraction (lower isocontours) corresponding to marginally supercritical successful initiation events in the three ignition modes identified in this study: a) mode 1: $\phi = 0.4$, $Re = 500$, $h = 0.1097$ mm, $Y_{H,max} = 9.728 \times 10^{-4}$; b) mode 2: $\phi = 0.4$, $Re = 250$, $h = 0.09726$ mm, $Y_{H,max} = 8.410 \times 10^{-4}$; and c) mode 3: $\phi = 0.7$, $Re = 100$, $h = 0.0187$ mm, $Y_{H,max} = 1.870 \times 10^{-3}$. For further details see caption of Fig. 3.
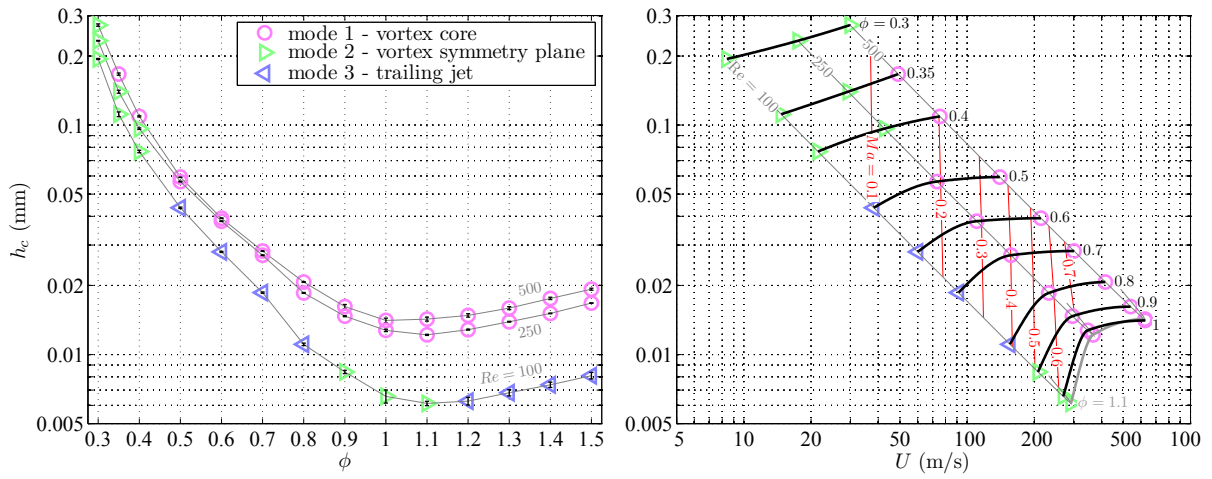
21

Figure 5: Variation of the critical slot semiwidth h_c with the equivalence ratio (left) and jet velocity (right). The left plot shows error bars indicating the marginal subcritical and supercritical values of h determined numerically, with h_c def ned as the average of both values. The right plot is limited to cases with $\phi \leq 1.1$. The ignition modes observed in the numerical integrations are indicated by the symbols specif ed in the f gure legend.

List of supplemental material

Supplementary videos

Filename: `Re=250_Phi=0.7_subcritical_Fig_3a.mp4`

Caption: Time evolution of the temperature and H-atom mass fraction in the failed initiation event shown in Fig. 3a for $Re = 250$ and $\phi = 0.7$.

Filename: `Re=250_Phi=0.7_supercritical_mode_1_Fig_3b.mp4`

Caption: Time evolution of the temperature and H-atom mass fraction in the successful initiation event (mode 1) shown in Fig. 3b for $Re = 250$ and $\phi = 0.7$.

Filename: `Re=500_Phi=0.4_supercritical_mode_1_Fig_4a.mp4`

Caption: Time evolution of the temperature and H-atom mass fraction in the successful initiation event (mode 1) shown in Fig. 4a for $Re = 500$ and $\phi = 0.4$.

Filename: `Re=250_Phi=0.4_supercritical_mode_2_Fig_4b.mp4`

Caption: Time evolution of the temperature and H-atom mass fraction in the successful initiation event (mode 2) shown in Fig. 4b for $Re = 250$ and $\phi = 0.4$.

Filename: `Re=100_Phi=0.7_supercritical_mode_3_Fig_4c.mp4`

Caption: Time evolution of the temperature and H-atom mass fraction in the successful initiation event (mode 3) shown in Fig. 4c for $Re = 100$ and $\phi = 0.7$.

Filename: `Re=100_Phi=1.1_supercritical_mode_2.mp4`

Caption: Time evolution of the temperature and H-atom mass fraction in a successful initiation event (mode 2) for $Re = 100$ and $\phi = 1.1$.

23